Research Article Vol. 34, No. 11 / 1 Jun 2026 / *Optics Express* 20790

Optics EXPRESS

Spatially dispersed virtual images in augmented reality by exploiting an electronic progressive liquid crystal lens

WEI-CHENG CHENG AND YI-HSIN LIN[*]

Department of Photonics, College of Electrical and Computer Engineering, National Yang Ming Chiao Tung University, Hsinchu, Taiwan
[*]*yilin@nycu.edu.tw*

Abstract: Visual fatigue, a discomfort of the eyes resulting from a distance mismatch between projected virtual images and surrounding real objects, is a major challenge in optically see-through augmented reality (AR) systems. To address it, we develop a spatially distributed projection of virtual images in an AR system by exploiting an electronic progressive liquid crystal lens (EPLC lens), which enables spatially multifocal wavefront modulation. The lens power in the EPLC lens is spatially dispersed and electrically adjustable. The operating principle is introduced. By adjusting the applied electric fields, the EPLC lens functions as a positive progressive lens and a negative progressive lens capable of adjusting projected images from 262 cm to 35 cm even though the lens power of the EPLC lens ranges only from +2 diopters to −1 diopters. The impacts of the proposed approach are not only in AR applications, but also in machine vision as well as advanced driver assistance systems.

1. Introduction

The virtual reality (VR) system projects computer-generated images into a virtual space to build an immersive virtual environment independent of the real world [1]. The augmented reality (AR) system projects digital images into the real world to enhance human perception of the real world [2]. I. E. Sutherland proposed the head-mounted display device or VR optical system in 1968 and researchers are trying to make the optical systems wearable and portable [2–7]. However, many technical challenges still need to be overcome [6–8]. One of main challenges is visual fatigue, a discomfort of eyes resulting from distance mismatch between accommodation cue and vergence cue. This is so-called vergence-accommodation conflict (VAC) [9]. In AR system, the distance mismatch between projected images and surrounding objects, so-called registration problem (or focus rivalry), results in another visual discomfort because crystalline lenses of eyes changing focal lengths all the time [4]. Many approaches are proposed to solve the visual discomfort. For example, computer generated holography (CGH) uses spatial light modulators (SLM) to simulate the light wavefront of real objects and tends to generate true 3D images directly [10,11]. However, the limitations are high computational cost as well as resolution caused by the diffraction of SLM pixel [10]. Light field approach and 3D integral imaging technology are trying to mimic light beams reflected from an object in order to generate quasi-3D images, but the resolution of images is limited by pixels of detectors and complementary metal-oxide-semiconductor (CMOS) sensors [12–15]. Reducing the difference between the accommodation cue and the vergence cue could improve the visual fatigue [16]. Such methods can be roughly divided into two types: varifocal and multifocal solutions [15,17–30]. We conclude that the underneath mechanisms are: time-multiplexing by adjusting the location of image planes for varifocal solution and creating multiple image planes at the same time for multifocal solution. This time-multiplexing approach requires a sufficient number of image planes to ensure acceptable perceived image quality for users [25]. These requirements result in extra-engineering challenges in component

#598784 https://doi.org/10.1364/OE.598784
Journal © 2026 Received 12 Mar 2026; revised 14 May 2026; accepted 14 May 2026; published 28 May 2026

design, device size, the power consumption and so on [19,26–28]. Liquid crystal (LC) lenses with tunable focal lengths are good candidates for varifocal solution in AR systems [31–35]. The optical mechanism of LC lenses is wavefront conversion as an incident polarized wave propagates through a LC layer within distributive optic axes or orientational arrangement of LC molecules [36,37]. Such distributive optic axes vary under applied electric fields. Several literatures are reported to apply liquid crystal lenses in AR system [7,23,24,38]. The position of the projected virtual image changes with different applied electric field [23,24,38]. However, we need to constantly change applied electric fields to a LC lens in order to project virtual images at different locations. The response speed of LC lenses is challenge. A question is then raised: is that possible to split the virtual images and then project at different locations at once under an applied electric field? To address this, the LC lens seems to be operated as a progressive lens with a spatially distributed lens power. Recently, we developed a tunable LC planar optics: electric freeform liquid crystal optics based on nematic liquid crystals capable of functioning as tunable progressive lenses, the non-uniform lens powers are able to be harnessed across the aperture [39]. The potential applications of such tunable progressive lenses in optical systems are still questionable. In this paper, we propose and demonstrate spatially dispersed virtual images in augmented reality by exploiting an electronic progressive liquid crystal (EPLC) lens. The wavefront modulations by the EPLC lens enables the optical system to project spatially dispersed virtual images. The operating principle of EPLC lens and how to apply a EPLC lens in an optical see-through AR system are first introduced. To proof-of concept, we also setup a simple demonstrate. The operating principle proposed in this paper is not only suitable for EPLC lens, but also could be apply to other optical devices as long as the optical devices exhibit the properties of progressive lenses.

2. Operating principle

LC optics is flat and the wavefront is modulated by the LC layer. It would be appropriate to introduce the optical mechanism based on wave optics, not geometrical optics. Here, we first extend the equation of the image formation based on wave optics when the wavefront is arbitrarily modulated by a lens. Assume we have a light source which is located at point A, and the corresponding image is formed at point B after light propagates through a lens (Fig. 1(a)). The objective distance and image distance are s_o and $s_{i,}$ respectively. Based on wave optics, the electromagnetic waves propagate right before and after the lens are expressed as two scalar waves: $U(r)$ and $U'(r)$, respectively. r equals to $\sqrt{x^2+y^2}$. The relation between $U(r)$ and $U'(r)$, linked by the transmittance function of the lens t_{lens}, is:

$$U'(r) = t_{lens} \cdot U(r). \tag{1}$$

Assume the lens modulates wavefront in an arbitrary way. The transmittance function of the lens t_{lens} equals to $e^{-jkW(r)}$, where k is wave vector and $W(r)$ is wavefront function or optical path difference (OPD). When the aperture size $(2r_0)$ of the lens is relatively small ($< 20\,\mathrm{mm}$), $U(r)$ and $U'(r)$ reasonably and approximately fitted by paraboloidal waves:

$$U(r) = A \cdot e^{+jk\frac{r^2}{2\cdot s_o}}. \tag{2}$$

$$U'(r) = A \cdot e^{+jk\frac{r^2}{2\cdot s_i}}. \tag{3}$$

Thus, from Eqs. (1)–(3) and expression of t_{lens}, we obtain generalization of image formation of a lens based on wave optics:

$$\frac{1}{s_o} + \frac{1}{s_i} = \frac{2}{r^2} \cdot W(r). \tag{4}$$

Conventionally the transmittance function has a quadratic phase related to focal length f under thin lens approximation, t_{lens} approximately equals to $e^{-jk\frac{r^2}{2\cdot f}}$ for a positive thin lens. In addition, the lens power, an inverse of focal length, equals to $1/r \cdot \partial W/\partial r$ [42]. As a result, Eq. (4) turns out the conventional equation of image formation in Geometrical Optics under the thin lens approximation: $1/s_o + 1/s_i = 1/f$.

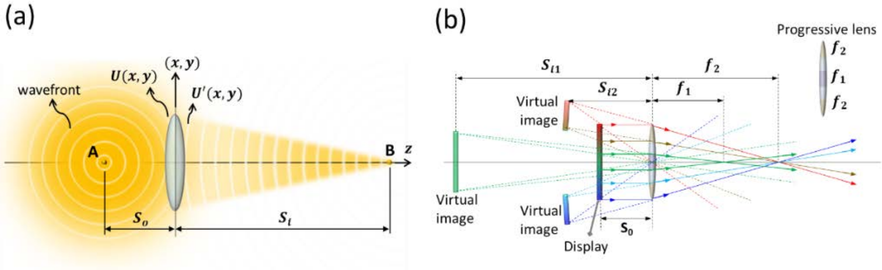

Fig. 1. Conceptual illustration of (a)image formation of a conventional lens and (b) spatially dispersed virtual images by a progressive lens. The focal lengths in the middle part and outside middle part of the progressive lens are f_1 and f_2 (f_1 <f_2,), respectively. The distance s_0 is smaller than f_1.

The wavefront function $W(r)$ in Eq. (4) is the product of refractive index n(r) and thickness of the lens (d(r)) (i.e.$W(r) = n(r) \cdot d(r)$). Typically, $W(r)$ is further decomposed as a linear superposition of Zernike polynomials. The Zernike coefficients in Zernike polynomials are related to different aberrations, such as spherical aberration, coma, astigmatism etc [42]. When $W(r)$ is an arbitrary function determined by designed optical elements, such as LC lenses, the LC lens then functions as a progressive lens which means the focal length is position-dependent (i.e., $f(r)$) [39]. When s_o<$f(r)$, $s_i(r)$<0 means the image is a virtual image and those virtual images spread at different locations. We rewrite Eq. (4) as:

$$s_i(r) = \frac{s_0(r)}{\frac{2 \cdot s_o(r)}{r^2} \cdot W(r) - 1}. \tag{5}$$

Equation (5) indicates that a progressive lens disperses virtual images to different image distances, as illustrated in Fig. 1(b). Assume the focal lengths of a lens in the middle region and other region are f_1 and f_2, respectively (Fig. 1(b)). When a display (e.g. micro-LED display) with self-emitted and collimated light is placed near the lens (s_o<f_1), three regions on a display corresponding to the regions of lens are formed three virtual images. The images on display split into three pieces and then spread to three locations. When the focal lengths of this lens are electrically tunable, the locations of the dispersed virtual images change as well.

Since LC molecules are flexible to be designed and modulate wavefront of incident light, it motivates us to propose an electronic progressive liquid crystal lens (EPLC lens) for the optical see-through AR system which enables spatially dispersed virtual images. The concept is illustrated in Fig. 2. In Fig. 2(a), the real images are projected at the same image plane for conventional lens as f<s_o<$2f$. In Fig. 2(b), the EPLC lens enables to projected real images to the different image planes when each region on the display corresponding to the lens area with different focal lengths. In Fig. 2(c), the spatially dispersed virtual images are projected by EPLC lens at the different image planes as s_0 less than the focal length. When the focal length of EPLC lens changes under applied electric field, the locations of virtual images changes accordingly. This is the basic optical principle of the spatially dispersed virtual images in augmented reality by exploiting an EPLC lens. The mechanism of the EPLC lens is based on physics of liquid crystals [40,41]. The distribution of molecular orientations of LC in the EPLC lens under applied electric fields is the equilibrium states by minimizing the total free energies, including Oseen-Frank elastic energy of material deformations, electric energy of applied electric fields, and surface anchoring energy at the boundaries. Any perturbations induced by the external stimuli disrupt the equilibrium and lead to another equilibrium state of the LC molecular orientations. The light speed of a polarized wave (i.e., extraordinary wave) varies with the LC molecular orientation as light propagates through the LC layer with a certain molecular orientation. As a result, the phase or the wavefront of the incident polarized light is modulated by the LC layer. When the wavefront of the incident polarized plane wave is converted to an aspherical wave, the incident plane light beam is converged or diverged. Thus, the LC layer functions as a positive lens or negative lens.

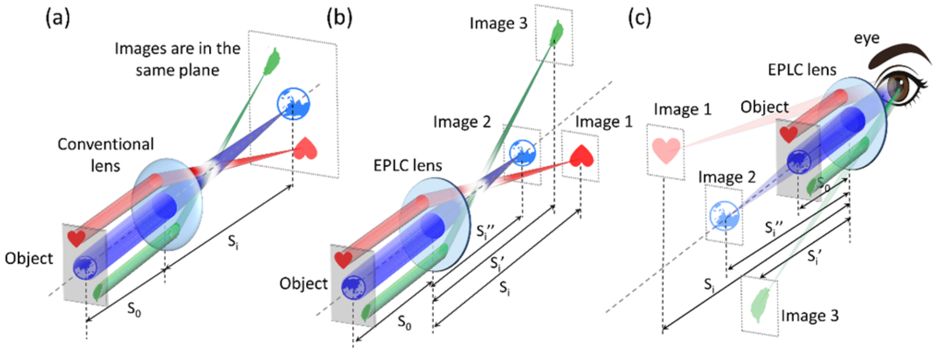

Fig. 2. (a) Illustration of image formation of conventional lens for $f < s_O < 2f$. f is focal length. The real images are projected at the same image plane. (b)The image formation of the EPLC lens. The focal lengths in the middle and other regions of EPLC lens are different. s_O is larger than the focal lengths. The images are still real images, but projected at the different image planes because of the spatially distributed focal lengths of the EPLC lens. (c) The image formation of the EPLC lens for s_O less than focal length. Eye sees the spreading virtual images at the different image planes.

3. Structure and sample preparation

To demonstrate the concept, we first design and fabricate the EPLC lens. The structure of the EPLC lens, cascaded GRIN LC lens, is depicted in Fig. 3(a). The function of the 1st LC lens is mainly to adjust the modulated wavefront and the 2nd LC lens is to modify the wavefront near the peripheral region. The EPLC lens consists of glass substrates, indium tin oxide (ITO), alignment layers, LC layers, insulating layers and high resistive layers. The upper part and the lower part of the cascaded GRIN LC lens in Fig. 3(a) are denoted as the 1st and 2nd LC lens, respectively. For the 1st LC lens, the hole-patterned ITO layer was deposited on a glass substrate with a thickness of 0.4 mm. A spin-coated high resistive layer (HRL) on the hole-patterned ITO layer was made of the conductive polymer (Dongjin Semichem Conducting Polymer DJCP series, Dongjin Semichem Co. Ltd) with a sheet resistance ~ 3MΩ/sq and a thickness <100 nm. The sheet ITO and hole-patterned ITO electrodes were separated with an insulating layer (NOA81, Norland) with a thickness of 35 µm. The mechanically rubbed alignment layers (polyvinyl alcohopolyvinyl) were coated on the opposite sides of the glass substrate with hole-patterned ITO electrode, as well as on the other sheet ITO glass substrate in order to align the LC molecules (nematic LC, MLC-2172, Merck, $\Delta n = 0.29$, λ=589.3 nm). The thickness of the LC layer is 100 µm controlled by a mylar film. As to the 2nd LC lens, the sample was fabricated by Innolux Corporation in Taiwan. The hole-patterned electrode of the 2nd LC lens was separated from the sheet ITO layer by an insulating layer (SiNx, thickness: 5700 Å). The HRL layer, which consists of indium oxide and silicon dioxide, was deposited via sputtering on the hole-patterned ITO layer. The sheet resistance and the thickness of HRL layer in 2nd LC lens are about 10 MΩ/sq and 33.5 nm. Mechanical rubbed alignment layers (polyvinyl alcohol) were coated on the substrates to ensure a homogeneous alignment of the LC mixture (MLC-2172). The LC thickness of the 2nd LC lens is 50 µm, controlled by the spherical spacers. The two LC lenses were tightly cascaded together as an EPLC lens. The apertures of both LC lenses are aligned precisely, and the aperture sizes ($2r_1$ and $2r_2$) are 10 mm.

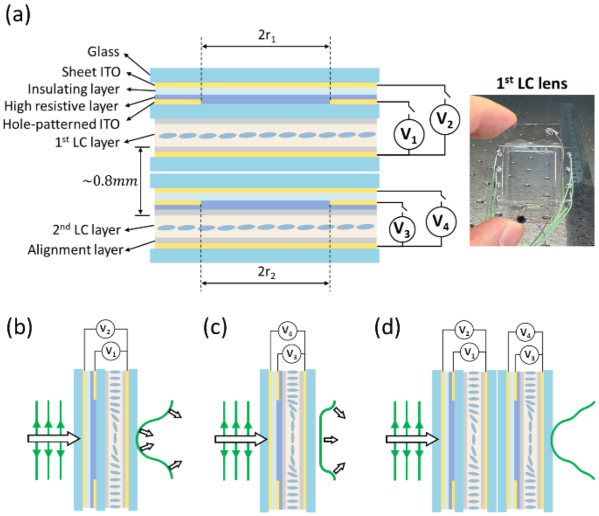

Fig. 3. (a) Illustration of the EPLC lens consisting of cascaded GRIN LC lens. We use a cascaded GRIN LC lens as an example to demonstrate the concept. (b) and (c) are the upper part (the 1st LC lens) and the lower part (the 2nd LC lens) in (a), respectively. The function of the 1st LC lens is mainly to adjust the modulated wavefront and the 2nd LC lens is to modify the wavefront near the peripheral region. (d) The outgoing wave is modulated by both of the 1st LC lens and the 2nd LC lens.

At voltage-off state, LC molecules of both LC layers are aligned parallel to the glass substrates. According to the modal lens theory, the electric field across the entire aperture is able to be estimated based on the model of a resistance-capacitance circuit [32]. The distribution of electric field is in the math form of a Bessel function depending on the applied voltages and frequencies. The frequency-dependent electric field stems from the HRL material's response. The electric field is frequency dependent due to the HRL material. We adjusted the electric signals or operating condition ($|V_1 - V_2| = |\Delta V|$ and frequencies) of the 1st LC lens. When the applied voltage ΔV is positive, the electric field in the peripheral region (i.e., $r = \pm r_1$ *or* $r = \pm r_2$) is larger than the central region (i.e., $r = 0$). The LC molecules in the peripheral region are more perpendicular to those in the central region. The refractive index of the LC layer for incoming the extraordinary wave (e-wave) varies gradually and remains spatially continuous across the whole aperture of the LC lens. The LC lens thereafter functions as a positive lens, which modulates the incident polarized plane wave to be a convergent aspherical wave, as depicted in Fig. 3(b). Similarly, the LC lens is operated as a negative lens at $\Delta V<0$, and the outgoing wave turns out a divergent aspherical wave. Even though the operating principle of the 2nd LC lens is identical to the first one, we specially operate the 2nd LC lens to modulate the incident wave at the peripheral region *only* (Fig. 3(c)) by properly choosing voltages and frequencies for the purpose of modification of the wavefront after the 1st LC lens. Neglecting the distances between the LC layers, the wavefront modulation of the EPLC lens is approximately equivalent to the linear combination of the wavefront modulation contributed by both LC lenses, as shown in Fig. 3(d). That means the modulated wavefront in Fig. 3(d) is the result of adding two modulated wavefronts in Fig. 3(b) and 3(c) together.

4. Experimental results and discussions

To measure the wavefront modulation of the EPLC lens, we set up a wavefront measurement system with Shack-Hartmann (SH) wavefront sensor (WFS150-7AR, Thorlabs). The light source of the wavefront measurement system consists of a He-Ne laser (λ=543 nm), a spatial filer (the object lens is 50x and pinhole size of 50μm), and a solid lens with a focal length of 50 mm to collimate the light beam. The collimated plane wave propagates through the EPLC lens and is relayed to the lens array of the SH wavefront sensor through a confocal beam expansion system consisting of two solid lenses ($f_1 = 50$ cm and $f_2 = 20$ cm). The EPLC lens is placed at the front focal plane of the first solid lens, while SH wavefront sensor is placed at the back focal plane of the second solid lens. As a result, the wavefront modulation of the EPLC lens, measured by SH wavefront sensor, is fitted with 66 Zernike polynomial terms [42]. The reconstructed wavefront (W) is expressed as $W = \sum\limits_{i=0}^{65} c_i \cdot Z_i$, where Z_i is Zernike polynomials and c_i is Zernike coefficient. The lens power of the wavefront (i.e., an inverse of the focal length, unit of m^{-1} or diopter) is then calculated and also expressed as $-c_4 \cdot 4\sqrt{3}/r_0^2$ under the parabolic wave assumption, where the r_0 is the radius of the aperture size. Figures 4(a) and 4(b) show the measured lens power as a function of applied voltages for the 1st and 2nd LC lenses, respectively. The lens powers of the 1st and the 2nd LC lens range from +2D to −2D and +1D to −1D, respectively. Both lenses are capable of being operated as either a positive lens or a negative lens. Two times difference in tunable range of the lens power is because of the thickness of the 2nd LC lens is only half of the 1st LC lens. The operating voltage of the 1st LC lens is higher than the 2nd LC lens due to the 0.4 mm thickness of the buffering layer in the 1st LC lens. From theoretical estimation, the maximum optical path differences modulated by two LC lenses are 29μm and 13.5μm, which quite agrees with the measurement results (27 μm and 12 μm). The slight difference might because the alignments of LC molecules in the central and peripheral regions are not perfectly parallel and perpendicular to the substrate.

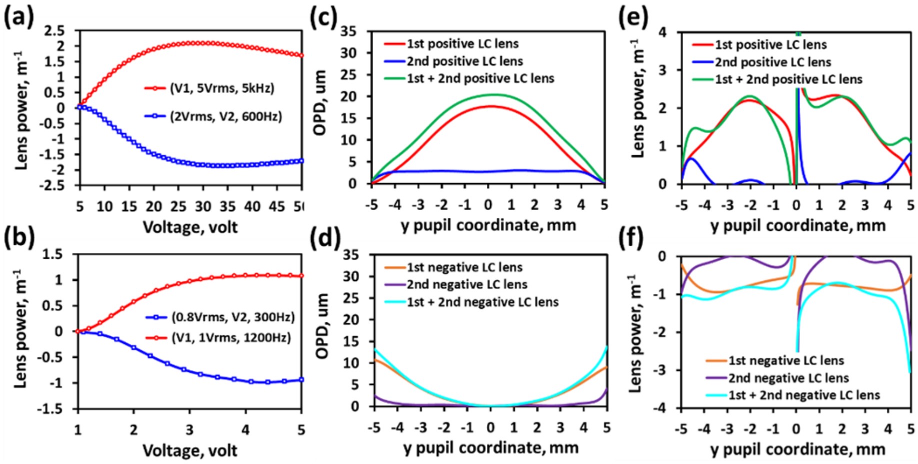

Fig. 4. The lens power as a function of applied voltage at different AC frequencies for the (a) 1st and (b) 2nd LC lenses. (c) The OPD v.s. y pupil coordinate contributed by the 1st LC lens only, 2nd LC lens only, and both of 1st and 2nd LC lenses (EPLC-1). (d) presents another set of OPD v.s. x pupil coordinate contributed by the 1st LC lens only, 2nd LC lens only, and both of 1st and 2nd LC lenses (EPLC-2). (e) and (f) are lens powers v.s. y pupil coordinate corresponding to (c) and (d), respectively.

The EPLC lens is operated as either a positive progressive lens or negative progressive lens. For the spatially multifocal purpose in our EPLC lens design, one of the sub-LC lenses is designed to function as a progressive LC lens and the other one is designed to modify the wavefront near peripheral region [39]. The main function of the 2nd LC lens is to shape the wavefront in the peripheral region to be more parabolic, thereby the lens power in peripheral region of EPLC lens is more uniform. In experiments, we selected two conditions to demonstrate the concept and we named the EPLC lens under two conditions as EPLC-1 and EPLC-2. The applied electric signals and corresponding Zernike coefficients for EPLC-1 and EPLC-2 are listed in Table 1. In EPLC-1 and EPLC-2, both of LC lenses are operated as either positive lenses or negative lenses. The measured OPDs v.s. the y pupil coordinate for EPLC-1 and EPLC-2 are shown as in Figs. 4(c) and 4(d). The red, blue and green lines in Figs. 4(c) and 4(d) stand for the OPD as only the 1st LC lens is on, only the 2nd LC lens is on, and both of lenses are on. In red line of Fig. 4(c), lens power of the 1st LC lens is ~1.4D estimated from Zernike coefficient c_4 and the maximum OPD is measured around 17.5 µm. As to the 2nd LC lens (blue line in Fig. 4(c)), the curve is pretty flat at $|r| \leq 4mm$, but decreases from $|r| = 4mm$ to $|r| = 5mm$. When both of lenses are on, it turns out the EPLC-1 we design and the corresponding OPD (green line) is the summation of red and blue lines in Fig. 4(c). One can see that the OPD goes higher at $4mm \leq |r| \leq 5mm$ compared to the red line at $4mm \leq |r| \leq 5mm$. Similarly, Fig. 4(d) depicted the measured OPD v.s. y pupil coordinate for the EPLC-2 lens as a negative lens when the 1st LC lens is on (red line), the 2nd LC lens is on (dark blue line), and both LC lenses (EPLC-2 lens) are on (light blue). The curve of 2nd LC lens is also pretty flat at the most of area, but near peripheral region ($4mm \leq |r| \leq 5mm$).

Table 1. The Zernike coefficients and operating electric signals for EPLC-1 and EPLC-2.

Zernike coefficient, [um]	Name	EPLC-1 (Positive lens)		EPLC-2 (Negative lens)	
		The first LC lens (35V_{rms}, 5V_{rms}, 4kHz)	The second LC lens (1.5V_{rms}, 1V_{rms}, 2kHz)	The first LC lens (2V_{rms}, 35V_{rms}, 100 Hz)	The second LC lens (1V_{rms}, 3.8V_{rms}, 300 Hz)
C_4	Defocus	5.145	0.524	−3.648	−0.636
C_{12}	1st spherical ab.	−1.078	0.377	0.34	−0.336
C_{24}	2nd spherical ab.	0.009	0.138	0.373	−0.14
C_7	1st y-coma	−0.158	−0.016	−0.003	0.065
C_8	1st x-coma	0.119	−0.072	0.006	−0.074
C_3	1st y-astigmatism	0.033	−0.024	−0.05	−0.001
C_5	1st x- astigmatism	0.005	−0.046	−0.003	−0.023

From Figs. 4(c) and 4(d), we calculated and depicted the lens power as a function of y pupil coordinate in Figs. 4(e) and 4(f). The lens power of the 1st LC lens (red line in Fig. 4(e)) is around 2 Diopter (D) at $1mm \leq |r| \leq 2mm$ which is higher than the theoretical calculated lens power of 1.4D estimated from the parabolic approximation. This difference is mainly due to large first-order spherical aberration induced the imperfect parabolic function of the OPD. The lens power of the 1st LC lens decreases from $r = \pm 2mm$ to the peripheral region (i.e., 0.3D at $r = \pm 5mm$). Besides, the lens power diverges as the r approaches to the origin because the lens power is inversely proportional to r. As a result, we conventionally ignore the region near $0 \leq |r| < 1mm$. At $0 \leq |r| < 4mm$, the lens power of the 2nd LC lens is approximately zero. The lens power goes up and down from $r = -4mm$ to $r = -5mm$, and increases from $r = 4mm$ to $r = 5mm$ The local maximum of the optical power is around 0.5 D at $r = -4.5\ mm$ and 0.6 D at $r = 5\ mm$. The uneven lens power is because of asymmetric wavefront. When we turn on both of lenses to be EPLC-1(green line), the lens power is ~ 2D in average at $|r| < 2.5mm$ and ~ 1.3D in average at $4mm < |r| < 5mm$. The lens power decreases from 2D to 1.3 D as $|r| = 2mm$ to $|r| = 4\ mm$. The more uniform the lens power distribution, the more parabolic the OPD profile. This means the lens satisfies parabolic approximation better and the aberration is lower which leads better images. The steeper slope in lens power from $|r| = 2mm$ to $|r| = 4\ mm$, the more non-uniform the magnification of an image. EPLC-1 has two regions for us to use in AR applications: 2D at $|r|<2.5mm$ and 1.3 D at $4mm<|r|<5mm$. Similarly, EPLC-2 has two regions for us to use in AR applications: −0.8D at $|r|<2mm$ and −1D at $3mm<|r|<4mm$.

The two-dimensional wavefronts (or OPD) v.s. xy-pupil coordinate for EPLC-1 and EPLC-2 are shown in Figs. 5(a) and 5(b). The corresponding lens power v.s. xy-pupil coordinate for EPLC-1 and EPLC-2 are also depicted in Figs. 5(c) and 5(d). The singular points in the center of Figs. 5(c) and 5(d) are the results of 1/r derivative relation of the optical power.($P_{lens} = 1/r \cdot \partial W/\partial r$) In Fig. 5(c) and 5(d), areas with uniform lens power for EPLC-1 and EPLC-2 are: 2D at $|r|<2mm$ and 1.3D at $4mm<|r|<4mm$, −0.8D at $|r|<2mm$ and −1D at $3mm<|r|<4mm$. In Figs. 5(a) to 5(d), we observed that the wavefront is more rotationally-asymmetric in EPLC-1 than EPLC-2. The rotationally-asymmetric wavefront is related to the coma aberration. From Table 1, the first-order coma aberration in the 1st LC lens is larger than the 2nd LC lens for EPLC-1. In addition, the 1st LC lens of EPLC-1 has larger first-order coma aberration than that of EPLC-2. As a result, the rotationally-asymmetric wavefront is mainly attributed to the contribution of the 1st LC lens. The question is what the root cause for the rotationally-asymmetric wavefront is. In our lens design, despite the electric field generated from the hole-patterned electrode is symmetric, the pretilt angle of LC molecules at V = 0 leads to uneven electric torques of LC molecules under electric fields [32,33]. This is the root cause of the phenomenon of the rotationally-asymmetric wavefront. From the rotationally asymmetric wavefronts, we are not surprised that the lens power distribution is also the rotationally asymmetric, as shown in Fig. 5(c) and 5(d). The average lens powers in Fig. 5(c) at the top, bottom, right, and left peripheral regions are around +1.1D, +1.4D, +1.2D, and +1.4D, respectively. Similarly, the lens power in Fig. 5(d) at the top, bottom, right, and left peripheral regions are around −1.7D, −1.8D, −1.9D, and −2.1D, respectively. In later application of augmented reality, we prefer the region with uniform lens power, instead of the region with large variations in lens power in Fig. 5(d). Figures 5(e) and 5(f) are calculated distributions of image distance $s_i(r, \theta)$ for EPLC-1 and EPLC-2 according to Eq. (5). In the calculation, the lens power of the solid lens is 20 Diopter which is used in the later AR system. The gap (~0.8 mm) between the two LC layers has to be considered because the object distance is very close to the focal length of the solid lens (~5 cm). In Fig. 5(e), the image distances are 92.5 cm, 107.5 cm, and 269.5 cm which are corresponding to three areas marked by the black dashed-line at the top, middle, and bottom, respectively. Similarly, in Fig. 5(f), the image distances are 35 cm, 40 cm, and 35 cm corresponding to three areas marked by the black dashed-line at the top, middle, and bottom, respectively. Those black dashed-line regions in Figs. 5(e) and 5(f) are used to demonstrate the spatially dispersed virtual image projection in AR system.

To proof-of-concept of the spatially dispersed virtual image projection with the electrically tunable EPLC lens, we setup a birdbath type AR system consisting of a micro-LED display (JBD, JBD5UM720PG, active area: 0.31”, resolution: 1280 × 720, 5000 ppi, λ=525 nm), the EPLC lens, a solid lens with a focal length of 50 mm, a beam splitter, and a camera (Canon, EOS 760D) to mimic a human eye, as illustrated in Fig. 6(a). The LC birefringence is given at 589.3 nm, the laser wavelength used for measurements is 543 nm, while the micro-LED wavelength is 525 nm. These minor differences should not affect the results too noticeably. An iris with an aperture size of 5 mm is placed in front of the camera in order to mimic the pupil of the eye. We aligned the aperture center of the EPLC lens with the solid lens and seamlessly integrated them as a projection lens set. A polarizer with the transmissive axis parallel to the rubbing direction is attached to the EPLC lens. The object length s_o, the distance between the micro-LED display and the solid lens, is set as 4.47 cm. When the EPLC lens is operated as a positive progressive lens, the effective focal length of the projection lens set would be longer than 4.47 cm. The objective

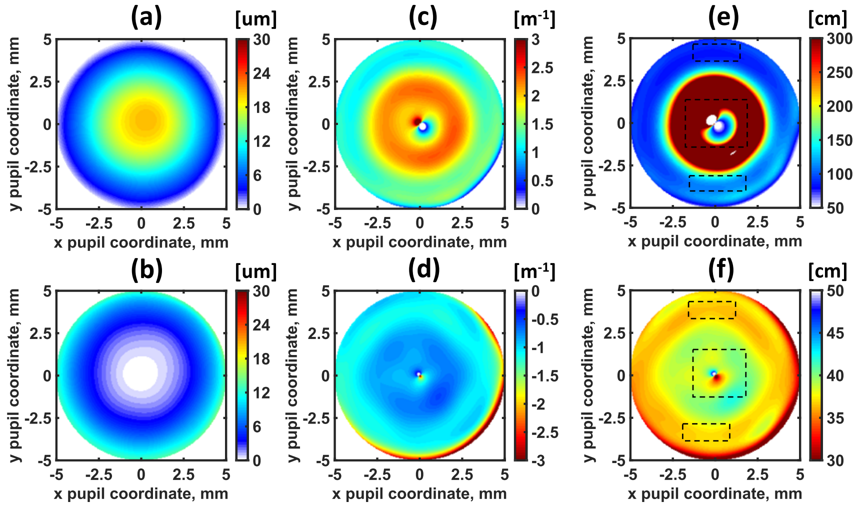

Fig. 5. (a) and (b) show two-dimensional OPD for EPLC-1 and EPLC-2, respectively. Color bar represents the OPD. (c) and (d) corresponds to lens power of (a) and (b). Color bar represents the lens power. (e) and (f) are calculated distributions of image distance $s_i(r, \theta)$ for EPLC-1 and EPLC-2 according Eq. (5). The solid lens with the lens power of 20 diopter is used to help shifting the lens power in the AR system.

distance must be less than the effective focal length of the projection lens set for the purpose of the formation of a virtual image. Thereafter, we prepared six targets to setup a scenario as illustrated in Fig. 6(a). Based on Figs. 5(e) and 5(f), 6 targets were placed at 35 cm, 40 cm, 50 cm, 85 cm, 100 cm, and 262 cm in front of the camera. The micro-LED display was aligned well with the projection lens as well as EPLC in order to make sure the camera see the real objects (i.e., the photos of “Taipei (85 cm)”, “The north lighthouse (262 cm)”, and “Sika deer (1 m)”) dispersed corresponding to the three regions marked by the dotted-line frames in Fig. 5(e). Initially, the lens power of the EPLC lens was zero, and the camera was set to see the object at 50 cm (i.e., pedestrians, the word of “50 cm” and green virtual images) at 50 cm (Fig. 6(b)). Then, when the EPLC lens was operated as the condition of EPLC-1, the camera still saw the object at 50 cm, but the virtual images turned out blurred because those virtual images changed the location (Fig. 6(c)). Thereafter, we adjusted the camera in order to see the object at 85 cm (direction sign) as well as the virtual image “Taipei (85 cm)”, but the other virtual images remained blurred (Fig. 6(d)). It indicates that both the virtual image “Taipei (85 cm)” and the direction sign are located at 85 cm and others are not. Then we adjusted the camera to see the photo of sika deer at 100 cm. The virtual image “Sika deer (1 m)” turned out clear at the same time. This means the virtual image “Sika deer (1 m)” is located at 100 cm (Fig. 6(e)). The virtual image of “The south lighthouse (262 cm)” and the photo of the lighthouse were clear when the camera was adjusted to focus at 262 cm (Fig. 6(f)). This represents that the virtual image is located at 262 cm. From Figs. 6(c)–6(f), the virtual images are located at different locations under the same electric signals. This shows that the EPLC lens, operated as a positive progressive lens (EPLC-1), projects one co-planar images at the micro-LED display into three separate virtual images at 85 cm, 100 cm, 262 cm away from the initial image plane (50 cm). Figure 6(g) and 6(h) show the magnified views of the regions marked by the red and blue frames in Fig. 6(d) and 6(e), respectively. “Taipei (85 cm)” is clearer in Fig. 6(g) and “Sika deer (1 m)” is clearer in Fig. 6(h). This also implies that the EPLC lens results in spatially dispersed virtual images located at different position.

Similarly, we operated the EPLC lens as a negative progressive lens (EPLC-2) to project images closer to the AR system. The experimental setup was the same, but different texts were

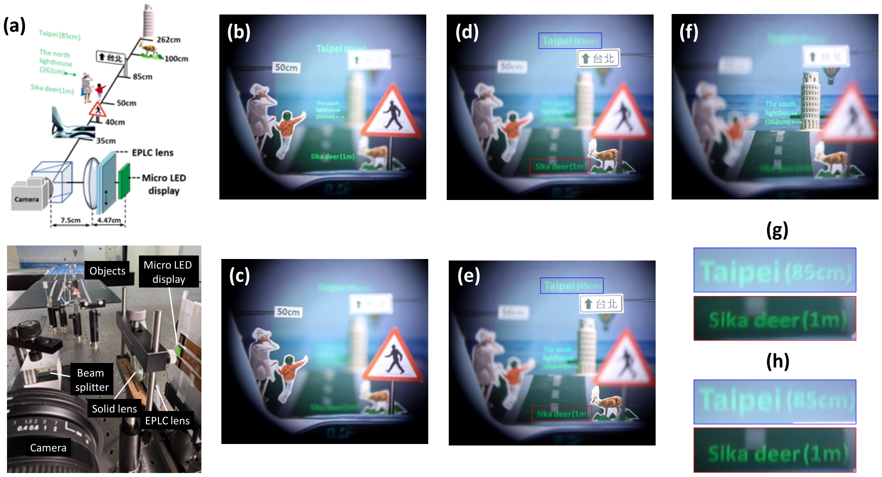

Fig. 6. (a) The experimental setup for AR demonstration. (b) The EPLC lens was off and the camera was set to focus at 50 cm. The projected virtual images, 'Taipei (85 cm)', 'The North Lighthouse (262 cm)', and 'Sika Deer (1 m)', were in three regions aligning with the three dotted-line frames in Fig. 3(e). The camera was used to mimic the human eye. (c) When the EPLC lens was operated as a positive progressive lens (EPLC-1), all virtual images turned out blurred because the virtual images were not at 50 cm. (d) When the camera was focused at 85 cm, the virtual image of 'Taipei (85 cm)' and the direction sign were clear. (e) When the camera was focused at 100 cm, the virtual image of 'Sika deer (1 m)' and the sika deer were clear. (f) When the camera was focused at 262 cm, the virtual image of 'The north lighthouse (262 cm)' and the lighthouse were clear. (g) and (h) are magnified images of the areas marked in the blue and red rectangles in (d) and (e), respectively. (See Visualization 1 for the operation from (b) to (f))

shown on the micro-LED display (Fig. 7(a)). When the EPLC lens was turned on, the virtual images were dispersed to 35 cm and 40 cm (Figs. 7(b) to 7(g)). In Figs. 8(a) to 8(e), we further test testing spatially continuous virtual image. When the EPLC lens was off, we setup virtual images and pedestrians at 50 cm (Figs. 8(b)). When the EPLC lens was operated as positive progressive lens (EPLC-1), the virtual images were blurred (Fig. 8(c)). By changing the focus of the camera at 100 cm and 262 cm, confirmed by "sika deer" and "light house", the virtual image was clear at the tail part and head part of the arrow with the text, respectively. This means the virtual image of the arrow is spatially continuous dispersed ranging from 100 cm to 262 cm.

By exploiting EPLC lenses into AR systems, we are able to project the information from a two-dimensional plane to a three-dimensional space. The method we proposed here has flexibility to be integrated with other technologies for providing versatile functionality, such as adding an extra polarization lens set for a speedy switch between two ranges of image distances [24]. Although the EPLC lens in our demonstration consists of two LC lenses, the pieces of LC lenses actually are not limited. The modulated wavefronts are able to be reshaped by means of adding extra LC lenses with different aperture sizes which leads to many segmented sub-wavefronts within uniform lens power. Because the aberrations of EPLC lenses are controllable, it can be used as an electrically tunable freeform optics components in optical imaging system to project the spatially dispersed images. The EPLC lens in this paper is polarization-dependent. The polarization-independent operation can be achieved by stacking two EPLC lenses with orthogonal alignment layers [43]. Depending on the application requirements, various designs configuration can be adopted to optimize the integration with specific light engine [44,45]. Conversely, chromatic aberration remains a significant challenge in AR/VR systems, especially

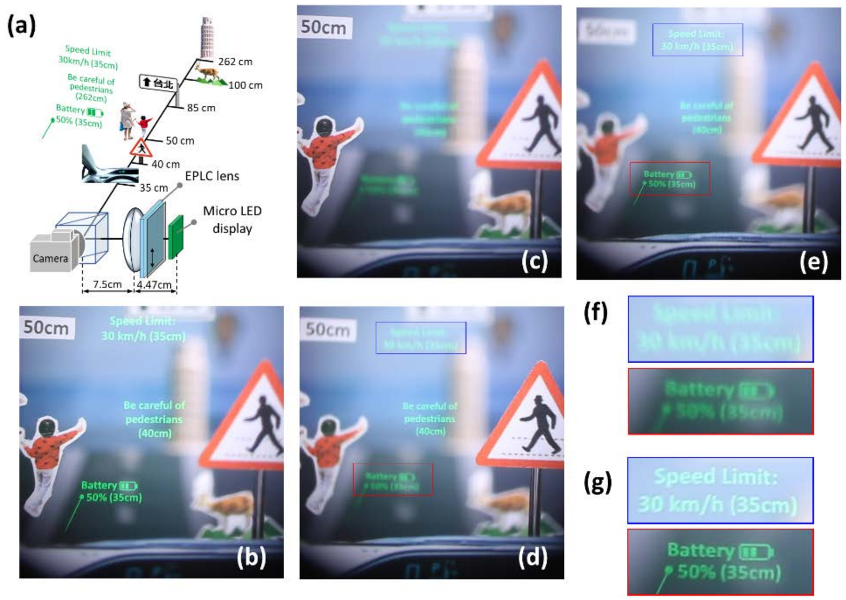

Fig. 7. (a) The setup of the AR imaging experiment, where the warning information 'Speed Limit 30 km/h (35 cm)', 'Be careful of pedestrians (40 cm)', and 'Battery 50% (35 cm)' in three distinct regions were displayed on the micro-LED display, corresponding to the three black-dashed frames in Fig. 5(f). (b) Deactivating the EPLC lens and setting the camera focus to 50 cm, the virtual images of warning information and pedestrians were positioned at the same depth, appeared sharp and clear, while the rest of the real-world scene remained blurred. (c) When the EPLC lens was operated as a negative progressive lens (EPLC-2), all virtual images turned out blurred because the virtual images were not at 50 cm anymore. (d) When the camera was focused at 40 cm, the virtual image 'Be careful of pedestrians (40 cm)' and the triangle sign were clear. (e) When the camera was focused at 35 cm, both of the virtual images: 'Speed Limit 30 km/h (35 cm)'and 'Battery 50% (35 cm)', and the dashboard were clear. (f) and (g) are magnified images marked in the blue and red rectangles in (d) and (e), respectively. (See Visualization 2 for the operation from (b) to (e))

for those utilizing the diffractive optics [46–48]. While the chromatic aberration of EPLC lens is inherently less than the diffractive lenses due to the spatially continuous wavefront modulation, the GRIN LC lenses still demonstrate stronger dispersion than conventional glass lenses [43,49]. Our recent studying indicates that the chromatic aberration of GRIN LC lenses can be mitigated by implementing an orthogonal alignment architecture [43]. The response time of the EPLC lens in this paper is approximately 90s arising from the $100\mu m$-thick LC layer. However, the proposed method, which simultaneously projects virtual images onto multiple focal planes, effectively compensates for this slow response time. When integrating the EPLC lens with full-color displays, computational pre-compensation emerges as a more preferable strategy to further mitigate chromatic aberration. While the glass substrate contributes most of the EPLC lens's weight and volume, adopting industrial LCD fabrication rather than laboratory prototyping enables a 4 mm aperture lens to weigh less than 0.05 g and volume below 0.02c.c. The ideal light beam from the display is collimated to avoid multiple images and image blur, therefore, the optimal size of the display is comparable with the EPLC lenses. When the light beams from the display are not perfectly collimated, the corresponding display area for the specific lens power region must be shrunken. This measure prevents the stray light of imperfect collimated beam from entering adjacent lens regions, which would otherwise result in ghost images caused by

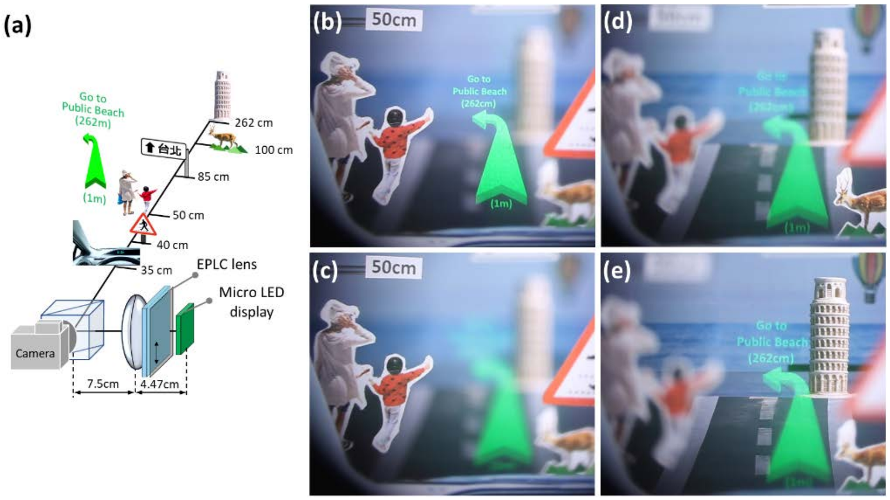

Fig. 8. (a) illustrates the experimental setup for testing spatially continuous virtual image. (b) When EPLC lens was off, we setup virtual image, pedestrians and triangle sign at 50 cm. (c) When EPLC lens was operated as positive progressive lens (EPLC-1), the virtual image was blurred. By changing the focus of the camera at (d)100 cm ("sika deer") and (e) 262 cm (light house), the virtual image was clear at the tail part and head part of the arrow with the text, respectively. (See Visualization 3 for the operation from (b) to (e))

different lens powers. When utilizing a non-collimated display source, a coded mask should be incorporated between the EPLC lenses and the observer to prevent the stray light from the display, but the tradeoff is the transmittance. Unlike pixelated modulators (e.g., SLMs [30] or microlens arrays [15]) that suffer from wavefront discontinuities, EPLC lenses provide continuous wavefront modulation ensuring the seamless projection of spatially dispersed virtual images. It is particularly important to the images requiring the reproduction of high-spatial-frequency details, as demonstrated in Fig. 7(g). Instead of projection, we could further apply the EPLC lens to sensing systems based on reciprocity of light or Helmholtz reciprocity: a real-time depth sensing. By a single snap shot of the camera or image sensor, the EPLC lens enables to help to calculate the distance of multiple objects at once. This would bring EPLC lens toward the great potential in optical sensing systems, not just projection systems.

5. Conclusion

A spatially distributed projection of virtual images in an AR system by exploiting an EPLC lens, which enables spatially multifocal wavefront modulation, was proposed and demonstrated. The general image formation as well as operating principle was introduced. By providing continuous wavefront modulation, EPLC lenses facilitate the seamless projection of two-dimensional information into three-dimensional space, effectively circumventing the wavefront discontinuities and digital artifacts common in pixelated modulators like SLMs. This capability is particularly critical for rendering high-spatial-frequency details, such as sharp text and intricate patterns, which are essential for high-fidelity information interaction. The operating principle proposed in this paper is not only limited in EPLC lens, but also could be applied for other optical devices as long as the optical devices exhibit the properties of tunable progressive lenses. The impact of this study is not only in AR systems, but also the great potential toward applications in advanced driver assistance systems (ADAS) and even machine vision.

Funding. National Science and Technology Council (114-2112-M-A49-011); Google (United States) (Google Gift).

Acknowledgments. The authors are indebted to Mr. Hao-Hsin Huang and Ms. Ting-Wei Huang in NYCU for technical assistance in optical measurement and photos. We specially thank Innolux Corp. (Taiwan) for helping fabrication of LC lenses.

Disclosures. WCC: Google LLC (R), YHL: Google LLC (R)

Data availability. Data underlying the results presented in this paper are not publicly available at this time but may be obtained from the authors upon reasonable request

References

1. M. L. Heilig, "Stereoscopic-television apparatus for individual use," U.S. patent 2,955,156 (4 October 1960).
2. I. E. Sutherland, "A head-mounted three dimensional display," *Fall Joint Computer Conference, 1968*, vol. 33, pp. 757–764 (1968).
3. R. J. Withrington, "Optical design of a holographic visor helmet-mounted display," Proc. SPIE 0147, Computer-Aided Optical Design, pp. 161–170 (1978).
4. R. T. Azuma, "A Survey of Augmented Reality," Presence **6**(4), 355–385 (1997).
5. G. Kramida, "Resolving the vergence-accommodation conflict in head-mounted displays," IEEE Trans. Vis. Comput. Graph. **22**(7), 1912–1931 (2016).
6. T. Zhan, K. Yin, J. Xiong, *et al.*, "Augmented reality and virtual reality: perspectives and challenges," iScience **23**(8), 101397 (2020).
7. Y. J. Wang and Y. H. Lin, "Liquid crystal technology for vergence-accommodation conflicts in augmented reality and virtual reality systems: a review," Liq. Cryst. Rev. **9**(1), 35–64 (2021).
8. K. Yin, Z. He, J. Xiong, *et al.*, "Virtual reality and augmented reality displays: advances and future perspectives," JPhys Photonics **3**(2), 022010 (2021).
9. D. M. Hoffman, A. R. Girshick, K. Akeley, *et al.*, "Vergence-accommodation conflicts hinder visual performance and cause visual fatigue," J. Vis. **8**(3), 33 (2008).
10. L. Shi, B. Li, C. Kim, *et al.*, "Towards real-time photorealistic 3D holography with deep neural networks," Nature **591**(7849), 234–239 (2021).
11. D. Blinder, T. Birnbaum, T. Ito, *et al.*, "The state-of-the-art in computer generated holography for 3D display," Light: Adv. Manuf. **3**, 572–600 (2022).
12. H. Huang and H. Hua, "Systematic characterization and optimization of 3D light field displays," Opt. Express **25**(16), 18508–18525 (2017).
13. H. Huang and H. Hua, "Effects of ray position sampling on the visual responses of 3D light field displays,".
14. B. Lee, "Three-dimensional displays, past and present," Phys. Today **66**(4), 36–41 (2013).
15. P. Y. Chou, J. Y. Wu, S. H. Huang, *et al.*, "Hybrid light field head-mounted display using time-multiplexed liquid crystal lens array for resolution enhancement," Opt. Express **27**(2), 1164–1177 (2019).
16. T. Shibata, J. Kim, D. M. Hoffman, *et al.*, "The zone of comfort: Predicting visual discomfort with stereo displays," J. Vis. **11**(8), 11 (2011).
17. C. K. Lee, S. Moon, S. Lee, *et al.*, "Compact three-dimensional head-mounted display system with Savart plate," Opt. Express **24**(17), 19531–19544 (2016).
18. Y. J. Wang, Y. H. Lin, O. Cakmakci, *et al.*, "Varifocal augmented reality adopting electrically tunable uniaxial plane-parallel plates," Opt. Express **28**(15), 23023–23036 (2020).
19. S. Liu, D. Cheng, and H. Hua, "An optical see-through head-mounted display with addressable focal planes," *Proc. IEEE/ACM Int'l Symp. Mixed and Augmented Reality (ISMAR '08)*, 33–42 (2008).
20. S. Liu and H. Hua, "Time-multiplexed dual-focal plane head-mounted display with a liquid lens," Opt. Lett. **34**(11), 1642–1644 (2009).
21. A. Wilson and H. Hua, "Design and demonstration of a vari-focal optical see-through head-mounted display using freeform Alvarez lenses," Opt. Express **27**(11), 15627–15637 (2019).
22. G. D. Love, D. M. Hoffman, P. J. W. Hands, *et al.*, "High-speed switchable lens enables the development of a volumetric stereoscopic display," Opt. Express **17**(18), 15716–15725 (2009).
23. Y. J. Wang, P. J. Chen, X. Liang, *et al.*, "Augmented reality with image registration, vision correction and sunlight readability via liquid crystal devices," Sci. Rep. **7**(1), 433 (2017).
24. Y. H. Lin, T. W. Huang, H. H. Huang, *et al.*, "Liquid crystal lens set in augmented reality systems and virtual reality systems for rapidly varifocal images and vision correction," Opt. Express **30**(13), 22768–22778 (2022).
25. S. Liu and H. Hua, "A systematic method for designing depth-fused multi-focal plane three-dimensional displays," Opt. Express **18**(11), 11562–11573 (2010).
26. J. P. Rolland, M. W. Krueger, and A. Goon, "Multifocal planes head-mounted displays," Appl. Opt. **39**(19), 3209–3215 (2000).
27. M. A. Reichow and D. M. Joseph, "Three dimensional display with multiplane image display elements," U.S. Patent 8,646,917, issued Feb. 11, 2014.
28. T. Zhan, J. Xiong, J. Zou, *et al.*, "Multifocal displays: review and prospect," PhotoniX **1**(1), 10 (2020).
29. W. Cui and L. Gao, "Optical mapping near-eye three-dimensional display with correct focus cues," Opt. Lett. **42**(13), 2475–2478 (2017).
30. N. Matsuda, A. Fix, and D. Lanman, "Focal surface displays," ACM Trans. Graph. **36**(4), 1–14 (2017).

31. S. Sato, "Liquid-crystal lens-cells with variable focal length," Jpn. J. Appl. Phys. **18**(9), 1679–1684 (1979).
32. M. Y. Loktev, V. N. Belopukhov, F. L. Vladimirov, *et al.*, "Wave front control systems based on modal liquid crystal lenses," Rev. Sci. Instrum. **71**(9), 3290–3297 (2000).
33. N. Bennis, T. Jankowski, P. Morawiak, *et al.*, "Aspherical liquid crystal lenses based on a variable transmission electrode," Opt. Express **30**(8), 12237–12247 (2022).
34. L. Tabourin, D. Brousseau, S. Thibault, *et al.*, "Wavefront control capability in a modal lens with segmented circular peripheral electrodes," Appl. Opt. **62**(30), 7970–7976 (2023).
35. L. Bégel and T. Galstian, "Dynamic presbyopia correction in the macular field of view by using a liquid crystal lens," Biomed. Opt. Express **16**(6), 2440–2458 (2025).
36. Y. J. Wang, Y. H. Lin, V. Reshetnyak, *et al.*, "Origin of oblique optical axis of electrically tunable focusing lenses arising from initial anisotropic molecular tilts under a symmetric electric field. I," AIP Adv. **10**(9), 095024 (2020).
37. Y. J. Wang, Y. H. Lin, O. Cakmakci, *et al.*, "Phase modulators with tunability in wavefronts and optical axes originating from anisotropic molecular tilts under symmetric electric field II: experiments," Opt. Express **28**(6), 8985–9001 (2020).
38. M. B. Kumar, D. Kang, J. Jung, *et al.*, "Compact vari-focal augmented reality display based on ultrathin, polarization-insensitive, and adaptive liquid crystal lens," Opt. Lasers Eng. **128**, 106006 (2020).
39. Y. H. Lin, W. C. Cheng, V. Reshetnyak, *et al.*, "Electrically tunable gradient-index lenses via liquid crystals: beyond the power law," Opt. Express **31**(23), 37843–37860 (2023).
40. P. G. de Gennes and J. Prost, *The Physics of Liquid Crystals*, 2nd ed. (Oxford University Press, 1993), chap. 3.
41. Y. H. Lin, Y. J. Wang, and V. Reshetnyak, "Liquid crystal lenses with tunable focal length," Liq. Cryst. Rev. **5**(2), 111–143 (2017).
42. G. M. Dai, *Wavefront Optics for Vision Correction* (SPIE, 2008), pp. 43–55.
43. Y. H. Lin, H. H. Huang, W. C. Cheng, *et al.*, "Polarization-independent electronically tunable liquid-crystal spectacles," Phys. Rev. Appl. **24**(2), 024071 (2025).
44. Y. Qian, Z. Yang, S.-C. Chen, *et al.*, "Power consumption of light engines for emerging augmented reality glasses: perspectives and challenges," Adv. Photonics **7**(03), 014001 (2025).
45. E. L. Hsiang, Z. Yang, P.-C. Lai, *et al.*, "AR/VR light engines: perspectives and challenges," Adv. Opt. Photonics **14**(4), 783–861 (2022).
46. T. Zhan, J. Zou, J. Xiong, *et al.*, "Practical Chromatic Aberration Correction in Virtual Reality Displays Enabled by Cost-Effective Ultra-Broadband Liquid Crystal Polymer Lenses," Adv. Opt. Mater. **8**(2), 1901630 (2020).
47. Y. Yang, J. Seong, M. Choi, *et al.*, "Integrated metasurfaces for re-envisioning a near-future disruptive optical platform," Light: Sci. Appl. **12**(1), 152 (2023).
48. Y. Ding, X. Huang, Y. Ma, *et al.*, "High-efficiency RGB achromatic liquid crystal diffractive optical elements," Opto-Electron. Adv. **8**(3), 240181 (2025).
49. J. Li, C. H. Wen, S. Gauza, *et al.*, "Refractive Indices of Liquid Crystals for Display Applications," J. Disp. Technol. **1**(1), 51–61 (2005).